Journal of Solid State Chemistry **144,** 330–338 (1999)
Article ID jssc.1999.8157, available online at http://www.idealibrary.com on IDEAL®

Differences and Similarities between the Isotypic Antimonides $M\mathrm{Fe}_{1-x}\mathrm{Sb}$, $\mathrm{ScCo}_{1-x}\mathrm{Sb}$, and $M\mathrm{NiSb}$ (M = Zr, Hf)

Holger Kleinke*,[1] and Claudia Felser†

*Fachbereich Chemie,. Philipps-Universität Marburg, D-35032 Marburg, Germany; †Institut für Anorganische Chemie und Analytische Chemie, Gutenberg-Universität Mainz, D-55099 Mainz, Germany
E-mail: kleinke@mailer.uni-marburg.de

Received October 13, 1998; in revised form December 24, 1998; accepted December 30, 1998

The new antimonides $M\mathrm{Fe}_{1-x}\mathrm{Sb}$ can be synthesized by arc-melting of M, Fe, and $M\mathrm{Sb}_2$ (M = Zr, Hf). All title compounds crystallize in the TiNiSi structure type (space group *Pnma*, Z=4). The lattice parameters of the new phases $M\mathrm{Fe}_{1-x}\mathrm{Sb}$, as obtained from the bulk samples of the nominal compositions *MFeSb*, are (a=681.4(1) pm, b=417.87(7) pm, c=740.3(1) pm for $\mathrm{ZrFe}_{1-x}\mathrm{Sb}$ and a=674.0(1) pm, b=412.0(2) pm, c=729.7(2) pm for $\mathrm{HfFe}_{1-x}\mathrm{Sb}$. Under the reaction conditions used, the occupancy factors of the iron position content of $\mathrm{ZrFe}_{1-x}\mathrm{Sb}$ does not exceed 68(1)% (i.e. x=0.32(1)). Extended Hückel calculations, performed on the hypothetical model structures "ZrFeSb" and "$\mathrm{ZrFe}_{0.75}\mathrm{Sb}$", point to the phase $\mathrm{ZrFe}_{1-x}\mathrm{Sb}$ being metallic, independent of the x value. The band structure of "ZrFeSb", obtained with *ab initio* LMTO calculations, reveals a three-dimensional metallic conductivity and a nonmagnetic ground state.

Key Words: **zirconium iron antimonide; preparation; structure and bonding; electronic structure.**

INTRODUCTION

Several ternary equiatomic antimonides were found to crystallize in the LiAlSi structure type. Recent results pointed out the existence of other structure types in these systems, namely the Ni_2In and TiNiSi type (an ordered variant of the Co_2Si structure type), the examples of which exhibiting different numbers of valence electrons (Table 1 (1–8). The electronic structures of the antimonides of the LiAlSi type exhibit a small band gap at the Fermi level with 18 valence electrons per formula unit. This was motivation for several investigations of the physical properties of these phases as well as of the analogous stannides (9–14). On the other hand, no band gap occurs in the vicinity of Fermi level of ScCoSb (2) or ZrNiSb (8).

Since the structure type may change by varying the valence-electron numbers, heavy doping of the antimonides in order to tune the physical properties should always be carried out along with structural investigations. Here we report on the structure of the hitherto unknown antimonides $\mathrm{ZrFe}_{1-x}\mathrm{Sb}$ and $\mathrm{HfFe}_{1-x}\mathrm{Sb}$ and concentrate on the phase range and electronic structure of $\mathrm{ZrFe}_{1-x}\mathrm{Sb}$ in comparison to related phases, including isotypic ZrNiSb and $\mathrm{ScCo}_{1-x}\mathrm{Sb}$.

EXPERIMENTAL

Synthesis

The phase $\mathrm{ZrFe}_{1-x}\mathrm{Sb}$ is accessible by arc-melting of Zr, $ZrSb_2$, and Fe in the ratio of 0.95 : 1.05 : 2, corresponding to an initial Zr Fe Sb ratio of 1 : 1 : 1.05. The elements Zr, Fe, and Sb were used in form of powders (Zr, ALFA, 4–20 mesh, purity 99.6%; Fe, Strem, 99.999%; Sb, Merck, 99.8%). $ZrSb_2$ was prepared first in order to avoid the use of elemental antimony in the arc-melter because of its comparably low boiling point of 1635°C. This was achieved in a reaction in a fused silica tube at 650°C, starting from the elements in the stoichiometric ratios. The mixture of Zr, $ZrSb_2$, and Fe was then pressed into a pellet and arc-melted twice under inversion in an argon atmosphere on a water-cooled copper hearth. Since the weight loss of 3 wt% is basically due to loss of antimony, the composition of the Zr Fe Sb reaction mixture is estimated to be 1 : 1 : 1.01. The powder diffractogram obtained from the ground sample of the product exhibited a reflection pattern very similar to that of ZrNiSb which crystallizes in the TiNiSi structure type. An analogous reaction using hafnium (Strem, powder, 99.6%, including up to 2.2% zirconium) instead of zirconium resulted in a similar powder diagram. The reflections of both powder diagrams were indexed based on the orthorhombic symmetry as found for TiNiSi (using silicon as internal standard and Cu$K\alpha$ radiation). The lattice dimensions obtained were a = 681.4(1) pm, b = 417.87(7) pm, c = 740.3(1) pm for

[1] To whom correspondence should be addressed.

0022-4596/99 $30.00

TABLE 1
Structure Types of Ternary Equiatomic Antimonides *MM′*Sb (*M*=Valence-Electron-Poor Transition Metal: *M′*=Fe, Co, Ni)

VE/*Z*[a]	LiAlSi type	TiNiSi type	Ni_2In type
17	TiFeSb (1)	ScCoSb (2)	—
18	ScNiSb (3), YNiSb (4), TiCoSb (1), ZrCoSb, HfCoSb (6), VFeSb, NbFeSb, TaFeSb (7)	—	LaNiSb (5) VFeSb[b] (7)
19	TiNiSb (1), VCoSb (1), NbCoSb, TaCoSb (7)	ZrNiSb, HfNiSb (8)	—
20	—	—	VNiSb (7)

[a] *VE*/*Z*: valence electrons per formula unit.
[b] High-temperature phase.

$ZrFe_{1-x}Sb$ and $a = 674.0(1)$ pm, $b = 412.0(2)$ pm, $c = 729.7(2)$ pm for $HfFe_{1-x}Sb$.

Structure Determination

In order to check the structure type and for the non-stoichiometry as found for $ScCo_{1-x}Sb$, a single crystal of the Zr containing sample was mounted on a glass fiber and thereafter used for a data collection on an IPDS diffractometer (Stoe). After correction of the data set for Lorentz and polarization effects and a numerical absorption correction (15), refinements (16) of the structure model taken from the structure solution of ZrNiSb converged smoothly to reasonable residual factors, confirming the supposition of the TiNiSi structure type. However, the relatively high displacement parameters of the Fe site ($U_{eq}(Fe) = 36(1)$ pm^2, $U_{eq}(Zr) = 9.7(6)$ pm^2, $U_{eq}(Sb) = 13.3(5)$ pm^2) indicate a not fully occupied Fe position. Correspondingly, a subsequent refinement of its occupancy factor resulted in 0.63(1) and a significantly lower $R(F)$ value of 0.032, compared to $R(F) = 0.055$ for the refinement with 100% occupancy of the Fe position. The enormous decrease of the R value of 42% cannot be just a consequence of better statistics (21 parameters refined instead of 20). No symmetry reductions or super structure reflections were observed.

To check for adventitious impurities, EDX investigations were performed using an electron microscope (Camscan, CS 4DV) with an additional EDX device (detector: Noran Instruments) on selected crystals. No impurities were found. While the Zr/Sb ratio of selected crystals was within $\pm 10\%$ of the stoichiometric 1:1 ratio, the Fe content varied between 24 and 30 at.%, which corresponds to a range of $0.10 \leq x \leq 0.27$, assuming the ideal Zr/Sb ratio, i.e. $ZrFe_{1-x}Sb$. However, these findings should be regarded cautiously, because the EDX results are somewhat uncertain for the following reasons: first, no standard was used, due to the lack of well-defined zirconium iron antimonides of the comparable stoichiometries; second, since iron occurs in a different period of the period table, compared to zirconium and antimony, the value obtained for iron are especially uncertain; and third, the results depend on the angle of the surface to the incident beam, and the crystals were rather irregular, e.g., the last problem is reflected in the variations of the Zr/Sb ratios obtained with the EDX measurements.

The question remained, why the crystals exhibited a stoichiometry different from the 1:1:1 starting ratio. An attempt to fill completely the Fe site of $ZrFe_{1-x}Sb$ was made by starting from a 30% excess of iron. Subsequent refinements of the single crystal structure obtained from a crystal of that sample resulted in the formula $ZrFe_{0.67(1)}Sb$. Even increasing the iron content to 240%, corresponding to the starting composition of 1 Zr:2.4 Fe:1.05 Sb, resulted in a similar product. Again, data collection was carried out on a single crystal of that sample, which yielded the formula $ZrFe_{0.68(1)}Sb$. Details of the three single crystal structure studies are listed in the Tables 2 and 3. Although the experimental results may be interpreted as a 2/3 occupancy of the iron position in all three cases investigated, we found no evidence for a tripling of any axis of the unit cell. Annealing at lower temperatures (900°C) over a period of 7 days did not lead to the occurrence of super structure reflections.

In a subsequent EDX investigation of the last case a Fe-rich phase was detected, which consisted of the elements Zr, Fe, and Sb roughly in the ratio of 1:4:1. Attempts to synthesize a significantly more Fe-deficient phase $ZrFe_{1-x}Sb$ failed: with initial compositions of $x > 0.5$, the yield of the $ZrFe_{1-x}Sb$ phase decreased with increasing x.

Band Structure Calculations

Semiempirical band structure calculations were performed using the extended Hückel approximation (17–19). The metal parameter were optimized using constant Sb parameters by alternating charge iteractions of the Zr and Fe ionization potentials until convergence (Table 4). The eigenvalue problem was solved in reciprocal space at 80 inequivalent k points. Since within the Hückel theory, non-stoichiometries cannot be handled, we used two models for the calculations, one with all four equivalent Fe atoms per unit cell, and one with only three equivalent Fe sites occupied, corresponding to the formulas "ZrFeSb" and "$ZrFe_{0.75}Sb$", respectively. The latter model serves as a simulation of the situation found experimentally ($ZrFe_{1-x}Sb$ with $x \approx 0.33$). For comparison, the model structure "$ZrNi_{0.75}Sb$" was calculated with the parameters used before (8).

TABLE 2
Selected Crystallographic Data for $ZrFe_{0.63(1)}Sb$, $ZrFe_{0.67(1)}Sb$, and $ZrFe_{0.68(1)}Sb$

Empirical formula	$ZrFe_{0.63(1)}Sb$	$ZrFe_{0.67(1)}Sb$	$ZrFe_{0.68(1)}Sb$
Molar mass	248.2 g/mol	250.4 g/mol	251.0 g/mol
Temp. of data collection	295 K	295 K	295 K
Crystal size/mm^3	$0.12 \times 0.08 \times 0.04$	$0.11 \times 0.07 \times 0.05$	$0.04 \times 0.02 \times 0.01$
Space group	*Pnma*	*Pnma*	*Pnma*
a/pm	682.7(2)	682.4(2)	681.2(2)
b/pm	417.9(1)	418.4(1)	418.5(1)
c/pm	739.9(2)	740.5(2)	741.4(2)
$V/(10^6$ pm$^3)$	211.1(1)	211.4(1)	211.4(1)
No. of f.u.; $F(000)$	4; 430	4; 434	4; 435
Calculated density	7.81 g/cm^3	7.87 g/cm^3	7.89 g/cm^3
Absorption coefficient	21.39 mm^{-1}	21.62 mm^{-1}	21.69 mm^{-1}
Range of 2θ	3°–60°	3°–60°	3°–60°
No. of measured reflections	1199	2262	1829
No. of independent reflections; R_{int}	344; 0.059	353; 0.066	352; 0.112
No. of observed relfections ($I > 2\sigma(I)$)	232	246	241
No. of parameters	21	21	21
Obs. refl.: $R(F)$, $R_w(F^2)$, GOF	0.032, 0.062, 0.86	0.030, 0.059, 0.98	0.038, 0.088, 0.99
Extinction coefficient	0.0000(9)	0.0028(6)	0.000(1)
Absorption correction	numerical	numerical	numerical
Min., max. transmission	0.29, 0.46	0.22, 0.34,	0.46, 0.85
Max., min., peak in final diff. map [e$^-$/(10^6 pm^3)]	1.89, − 1.68	2.09, − 2.17	3.10, − 2.48

Ab initio calculations were done using the self-consistent TB-LMTO-ASA program within the local density approximation (20–22). The integration in k space was performed by the tetrahedron method (23) on a grid of 1331 irreducible k points. The 4*f* orbitals of zirconium and antimony were included by sing a downfolding technique.

RESULTS AND DISCUSSION

Crystal Structure

$ZrFe_{1-x}Sb$ and $HfFe_{1-x}Sb$ crystallize in the TiNiSi structure type, an ordered variant of the Co_2Si type. The unit cell volume of the Hf containing antimonide is 4.0% smaller than that of $ZrFe_{1-x}Sb$, which is a consequence of the smaller radius of Hf, compared to Zr. A similar difference of 3.3% was found between the unit cell volumes of ZrNiSb and HfNiSb (8). The crystal structure of $ZrFe_{1-x}Sb$ is shown in Fig. 1, with emphasis on the (distorted) trigonal Zr_4Fe_2 prisms. These prisms are interconnected via the triangular faces to form linear chains parallel to the crystallographic b axis, and the chain are connected via common edges to puckered sheets. However, $ZrFe_{1-x}Sb$ should not be considered as a typical layered compound, because the sheets are combined to a three-dimensional network by

TABLE 3
Atomic Positions and Displacement Parameters [10^4 pm^2] for $ZrFe_{1-x}Sb$[a]

Atom	x	z	U_{11}	U_{22}	U_{33}	U_{13}	U_{eq}
Zr[b]	0.0006(1)	0.7920(2)	0.0091(4)	0.0115(6)	0.0122(6)	0.0010(4)	0.0109(3)
Zr[c]	0.0010(2)	0.7926(1)	0.0098(4)	0.0149(5)	0.0101(5)	0.0005(4)	0.0116(3)
Zr[d]	0.0013(2)	0.7929(2)	0.0103(6)	0.0157(8)	0.0114(7)	0.0004(5)	0.0124(4)
Fe[b]	0.1557(3)	0.4254(4)	0.011(1)	0.010(2)	0.012(2)	0.000(1)	0.011(1)
Fe[c]	0.1554(3)	0.4258(3)	0.013(1)	0.015(1)	0.008(1)	− 0.0009(9)	0.0117(9)
Fe[d]	0.1537(4)	0.4269(4)	0013(2)	0.014(2)	0.011(2)	− 0.001(1)	0.013(1)
Sb[b]	0.2776(1)	0.0929(1)	0.0092(3)	0.0179(5)	0.0170(4)	− 0.0017(3)	0.0147(3)
Sb[c]	0.2773(1)	0.0939(1)	0.0104(3)	0.0211(4)	0.0139(4)	− 0.0013(3)	0.0151(3)
Sb[d]	0.2771(1)	0.0946(2)	0.0109(5)	0.0210(6)	0.0175(5)	− 0.0016(4)	0.0165(4)

[a] All atoms on Wyckoff position 4*c*, $y = \frac{1}{4}$, $U_{12} = U_{23} = 0$.
[b] $ZrFe_{0.63(1)}Sb$; occupancy of Fe site: 0.63(1).
[c] $ZrFe_{0.67(1)}Sb$; occupancy of Fe site: 0.67(1).
[d] $ZrFe_{0.68(1)}Sb$; occupancy of Fe site: 0.68(1).

TABLE 4
Parameters Used for the EH Calculations

Orbital	H_{ii}/eV	ζ_1	c_1	ζ_2	c_2
Zr, 5*s*	− 8.31	1.82			
Zr, 5*p*	− 4.72	1.78			
Zr, 4*d*	− 8.32	3.84	0.6213	1.510	0.5798
Fe, 4*s*	− 7.92	1.90			
Fe, 4*p*	− 3.89	1.90			
Fe, 3*d*	− 9.24	5.55	0.5366	1.800	0.6678
Sb, 5*s*	− 18.80	2.32			
Sb, 5*p*	− 11.70	2.00			

Zr–Zr, Zr–Fe, Zr–Sb, and Fe–Sb bonding interactions (see discussion of the electronic structure).

From a local point of view, each Sb atom is surrounded maximally by nine metal atoms (five Zr and up to four Fe atoms, i.e. averaged 2/3 of four Fe) in form of a three-capped trigonal prism (tetrakaidecahedron), whereas the Zr atoms are coordinated by six Sb atoms in form of a severely distorted octahedron (5 + 1 coordination, see Table 5) and the Fe atoms are tetrahedrally coordinated by four Sb atoms. The five shorter Zr–Sb bonds, ranging from 292.1(2) to 297.1(1) pm, are about 10 pm longer than the corresponding sums of the Pauling radii ($r_{Zr} + r_{Sb} = 145$ pm + 13 pm = 284 pm (24). On the other hand, even the average of the Fe–Sb bonds (253 pm) is shorter than the sums of the radii ($r_{Fe} + r_{Sb} = 117$ pm + 139 pm = 256 pm), which may in part be a consequence of the low occupancy of the Fe site. Homoatomic metal–metal, especially Zr–Zr, bonds do also play a role for the stability of $ZrFe_{1-x}Sb$ (i.e. $d_{Zr-Zr} =$ 347.0(2) pm), whereas the shortest Sb–Sb distances (being longer than 390 pm) are too long for significant interactions.

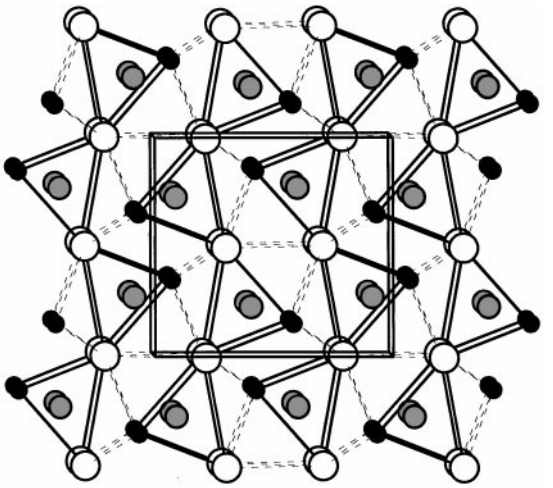

FIG. 1. Structure of $ZrFe_{1-x}Sb$ in a projection along [010]. Horizontal: *c* axis. Small, black circles, Fe; medium, gray circles, Sb; large, white circles, Zr atoms. Only metal–metal bonds are shown, emphasizing the (distorted) trigonal Zr_4Fe_2 prisms.

TABLE 5
Selected Interactions for $ZrFe_{0.63}Sb$ and ZrNiSb

Interaction[a]		Multi.	Length[b]/pm	*MOP*[c]	*MOP*[d]	length[e]/pm	*MOP*[e]	*MOP*[f]
Zr	Zr	2×	347.0(2)	0.105	0.114	345.3(1)	0.151	0.153
Zr	Zr	2×	372.0(1)	0.090	0.090	362.75(9)	0.127	0.123
Zr	Zr	2×	417.9(1)	0.014	0.017	415.87(8)	0.026	0.028
Zr	*M*′	2×	284.4(2)	0.215	0.216	291.31(7)	0.100	0.098
Zr	*M*′	1×	291.2(3)	0.164	0.176	304.5(1)	0.063	0.062
Zr	*M*′	1×	314.9(3)	0.110	0.105	311.92(9)	0.057	0.056
Zr	*M*′	2×	329.3(2)	0.084	0.082	313.8(1)	0.048	0.047
Zr	Sb	1×	292.1(2)	0.367	0.393	291.44(7)	0.410	0.429
Zr	Sb	2×	294.9(1)	0.325	0.352	295.01(6)	0.357	0.377
Zr	Sb	2×	297.1(1)	0.288	0.322	296.65(6)	0.346	0.370
Zr	Sb	1×	322.9(2)	0.126	0.154	332.12(7)	0.129	0.149
M′	Sb	2×	247.2(2)	0.309	0.313	248.58(6)	0.230	0.230
M′	Sb	1×	258.5(3)	0.238	0.245	253.88(8)	0.199	0.197
M′	Sb	1×	259.7(3)	0.254	0.246	261.7(1)	0.161	0.164
M′	*M*′	2×	317.9(2)	0.003	0.005	339.6(1)	− 0.009	− 0.008
Sb	Sb	2×	393.4(1)	− 0.004	− 0.005	381.15(9)	− 0.006	− 0.006

[a] *M*′ = Fe, Ni.
[b] $ZrFe_{0.63}Sb$.
[c] Mulliken overlap populations, obtained from the EH calculations on the model "ZrFeSb."
[d] Obtained from the EH calculations on the model "$ZrFe_{0.75}Sb$."
[e] Obtained from the EH calculations on ZrNiSb.
[f] Obtained from the EH claculations on the model "$ZrNi_{0.75}Sb$."

Electronic Structure

A comparison between the densities of states of the model structures "ZrFeSb" and "$ZrFe_{0.75}Sb$", calculated with the Extended Hückel approximation, is given in Fig. 2. The lower part of the figure exhibits the 5p peak of antimony between -15 and -12 eV, with some contribution of iron and zirconium, due to the covalence of the Fe–Sb and Zr–Sb interactions. The conduction band, starting above -10.5 eV, consists of the *d* states of zirconium and iron, with the iron peak centered around -9.3 eV. The iron and zirconium states clearly overlap, as was observed for the nickel and zirconium states in case of ZrNiSb, also. The different Fe content does not result in significant differences in the densities of states, aside from the height of the Fe peak well below the Fermi level at -8.44 eV ("ZrFeSb") or -8.49 eV ("$ZrFe_{0.75}Sb$"). In any case, a significant density of states is found at the Fermi level.

Basically the same picture results from the *ab initio* calculations (left part of Fig. 3). The most significant difference occurs at the 5*p* block of antimony, which is not well separated from the conduction band in case of the more reliable LMTO method. The differences in the region of the Fermi level are rather negligible, which supports the reliability of the semiempirical extended Hückel method. To check if we can exclude a magnetic ground state, we performed also a spin-polarized calculation within the local spin density approximation. The self-consistent calculation leads to an nonmagnetic ground state, therefore we expect a Pauli paramagnetic behaviour for the compound. The band structure shown on the right part of Fig. 3 emphasizes that "ZrFeSb" should exhibit three-dimensional metallic properties, since several bands cross the Fermi level along almost all symmetry directions (25) shown, including i.e. Γ–*X*, Γ–*Y*, and Γ–*Z* which are parallel to the axes of the reciprocal unit cell.

In order to show the character of the bands responsible for the metallic conduction, we use the fat band representation in Fig. 4. While the DOS revealed that iron and zirconium *d* states predominate the conduction band, Fig. 4 shows that the Zr contributions are almost negligible, compared to the Fe *d* character of the band involved. This furthermore implies that the precise character of the bands crossing the Fermi level strongly depends on the Fe substoichiometry, which was neglected in the calculation. Therefore, we expect that the Fermi level occurs at somewhat lower energies while the dispersions of the Fe *d* bands may vary, also.

To obtain more information about the influence of the substoichiometry on the bonding situation, we calculated the crystal orbital overlap populations (COOP curves) (26) and crystal orbital Hamilton populations (COHP curves) (27), respectively, for all different kinds of interactions of importance in the structure of $ZrFe_{1-x}Sb$. The metal–metal COOP curves, i.e. Zr–Zr, Zr–Fe, and Fe–Fe, interactions as obtained for the two model structures "ZrFeSb" and "$ZrFe_{0.75}Sb$" are depicted in Fig. 5. First of all, only bonding Zr–Zr states are filled in the average over the first Brillouin zone, whereas both interactions with iron contribution considered here consist in part of antibonding states. In the Fe-deficient model structure, more bonding Zr–Zr states are filled, and—of course, fewer Fe–Fe and Zr–Fe states—summed over the whole unit cell. (Note that the curves shown in Figs. 5–8 are the sums of the corresponding interactions within the unit cell.)

Again, no significant differences are found between the results of the Hückel and the LMTO method (Fig. 6),

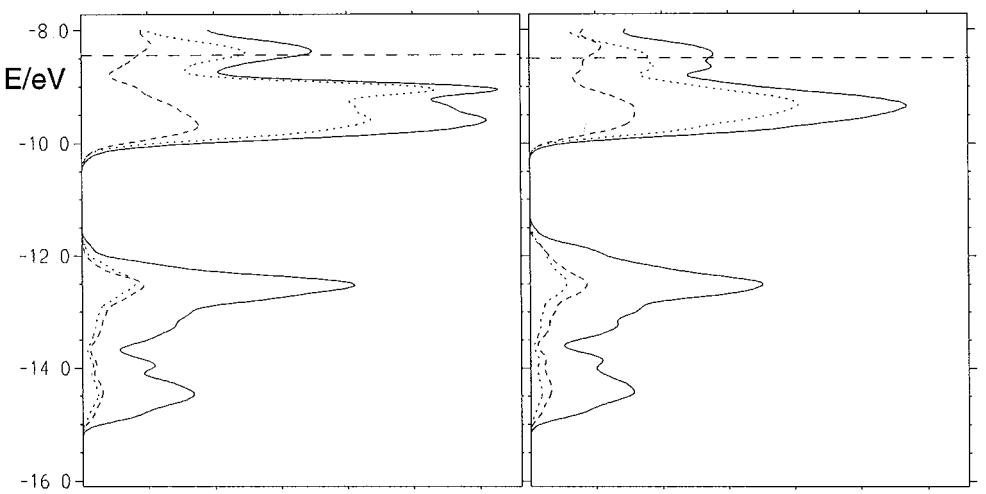

FIG. 2. Densities of states for "ZrFeSb" (left) and "$ZrFe_{0.75}Sb$" (right) (EH results). Dashed horizontal lines: Fermi levels. Solid lines, total DOS; dashed lines, Zr; dotted lines, Fe contributions.

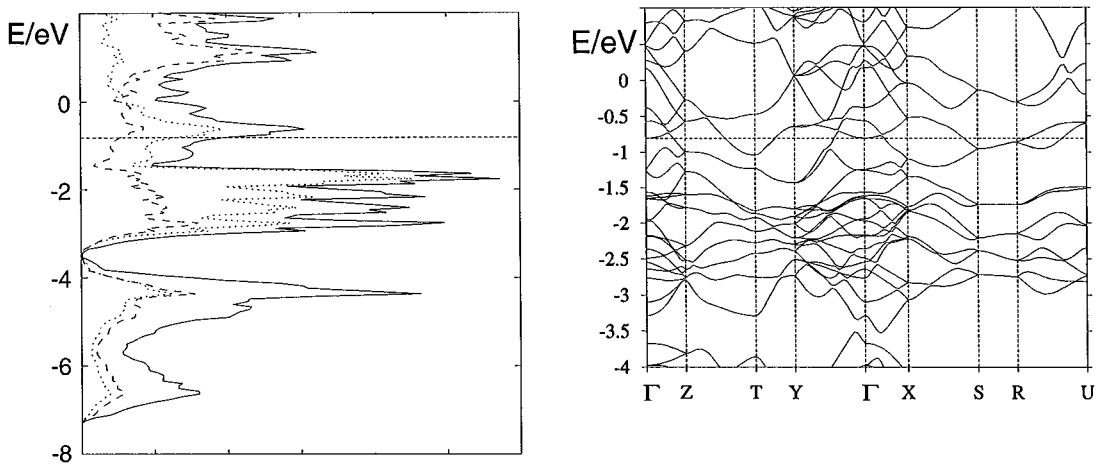

FIG. 3. Densities of states (left) and band structure (right) of "ZrFeSb" (LMTO method). Left: solid lines, total DOS; dashed lines, Zr; dotted lines, Fe contributions. Right: symmetry points, $\Gamma = (0, 0, 0)$; $Z = (0, 0, \frac{1}{2})$; $T = (0, \frac{1}{2}, \frac{1}{2})$; $Y = (0, \frac{1}{2}, 0)$; $X = (\frac{1}{2}, 0, 0)$; $S = (\frac{1}{2}, \frac{1}{2}, 0)$; $R = (\frac{1}{2}, \frac{1}{2}, \frac{1}{2})$; $U = (\frac{1}{2}, 0, \frac{1}{2})$ in units of the reciprocal lattice.

although the crystal orbital Hamilton populations are defined in a different way: whereas the COOP curves result from weighing the densities of states according to Mulliken's population analysis, which is an electron-partitioning scheme, the Hamiltonian matrix H is used to calculate the COHP terms (26, 27).

The Mulliken Overlap Populations of each bond are listed in Table 5 (*MOP*s, given in electrons per bond, as calculated within the extended Hückel approximation). The values confirm the net bonding character of all Zr–Zr and Zr–Fe interactions. In average, all metal–metal bonds are stronger in case of the Fe-deficient model structure "$ZrFe_{0.75}Sb$", compared to hypothetical "ZrFeSb", which may be a hint for the necessity of the substoichiometry. For comparison, the corresponding values of ZrNiSb and the model structure "$ZrNi_{0.75}Sb$" are also listed in Table 5. In contrast to the Fe-containing models, the averaged Zr–Ni bonds are weaker in case of the model with the deficiency, but the trend for the Zr–Zr interactions is the same as calculated for $ZrFe_{1-x}Sb$. One further significant difference between the electronic structures of "ZrFeSb" and ZrNiSb is the interaction between the 3*d* metal atoms M': in case of $M' = Fe$, a small net positive overlap population (0.003) results, whereas in case of $M' = Ni$ the net overlap population is negative (-0.009). This is assumed to be a consequence of the filled *d* states of nickel, which reflect themselves in a larger Ni–Ni separation of 339.6(1) pm, compared to $d_{Fe-Fe} = 317.9(2)$ pm (despite of $r_{Ni} = 115$ pm $< r_{Fe} = 117$ pm). Similarly, the Co–Co distance is 314.6(2) pm in $ScCo_{0.75}Sb$ and 315.1(2) pm in $ScCo_{0.93}Sb$, while the sizes of the Zr and Sc atoms ($r_{Sc} = 144$ pm) are comparable.

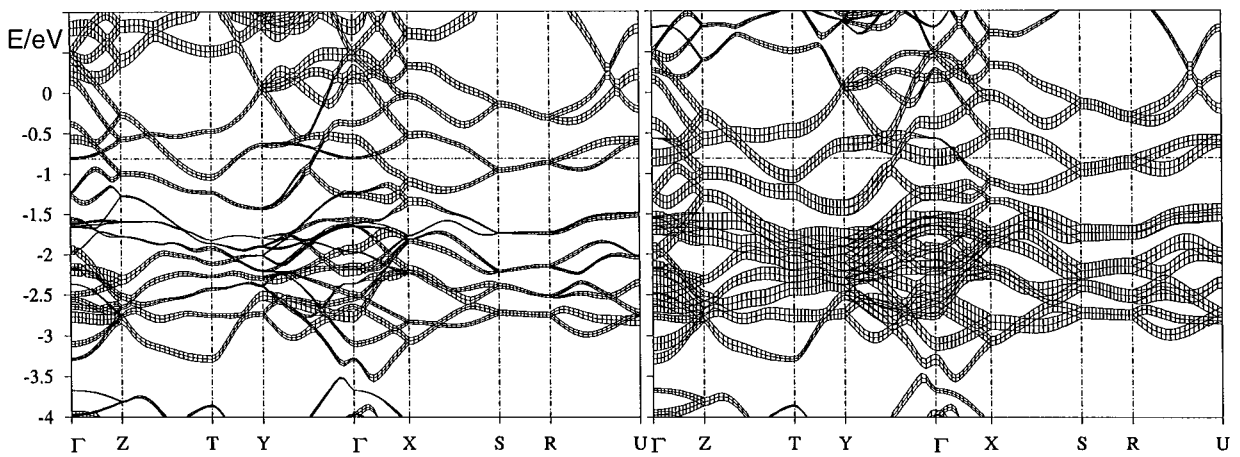

FIG. 4. Band structure of "ZrFeSb" (LMTO method), emphasizing via fat bands the Zr *d* bands (left) and the Fe *d* bands (right), respectively.

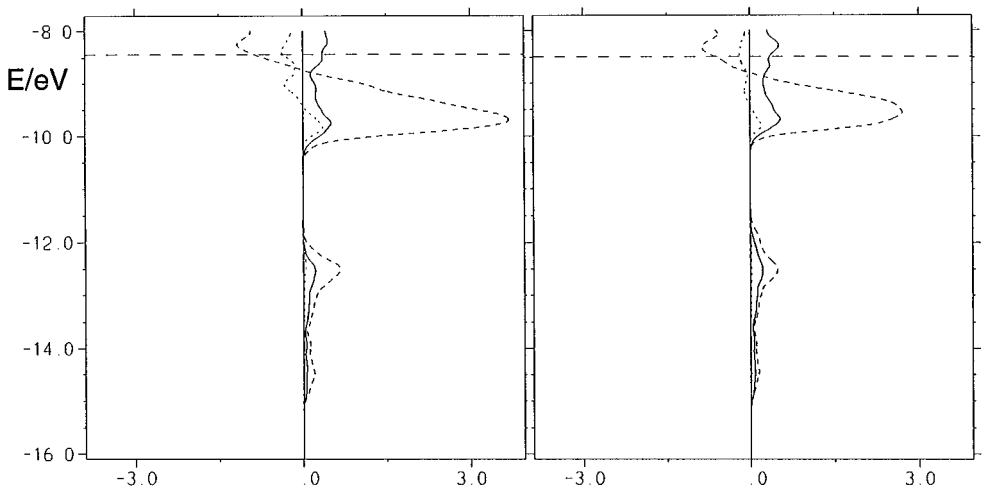

FIG. 5. Summed crystal oribital overlap populations (COOP) for "ZrFeSb" (left) and "$ZrFe_{0.75}Sb$" (right) (EH results). Horizontal lines: Fermi levels. Solid line, Zr–Zr; dashed line, Zr–Fe; dotted lines, Fe–Fe interactions. Left, antibonding (−); right, bonding (+).

Based on the experiments, however, one might assume that the possibility of full occupancy of the M' sites increases with decreasing size of the M' atoms, if one compares $ZrFe_{0.68}Sb$, $ScCo_{0.93}Sb$, and $ZrNi_{1.0}Sb$. This statement seems to be too general for two reasons: first, the phase range of $ScCo_{1-x}Sb$ was not determined, second, single crystal structure studies on related phosphides and arsenides, which also crystallize in the TiNiSi type, resulted in the formulas $HfCo_1As$ (28) and $HfNi_{0.90}P$ (29) with shorter M'–M' distances of 279.5(2) and 276.4(5) pm, respectively.

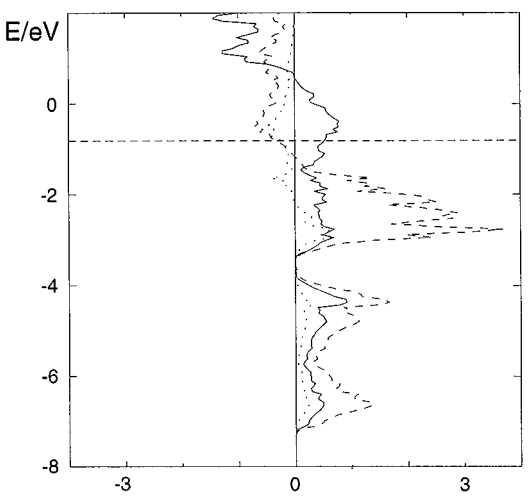

FIG. 6. Summed crystal orbital Hamilton populations (–COHP) for "ZrFeSb" (LMTO results). Horizontal line: Fermi level. Solid line, Zr–Zr; dashed line, Zr–Fe; dotted line, Fe–Fe interactions. Left, antibonding (–); right, bonding (+).

The metal–antimony bonds are depicted in Figs. 7 and 8. According to the results of both calculation methods, the Zr–Sb interactions consists only of filled bonding states, which are not optimized at the Fermi level. On the other hand, some antibonding states of the Fe–Sb interactions are filled, but thse interactions still have net bonding character. Again, the overlap populations per bond are larger in case of "$ZrFe_{0.75}Sb$", compared to "ZrFeSb". The same trend holds for a comparison of ZrNiSb with "$ZrNi_{0.75}Sb$", but it is not as strong. Averaged over all Zr–Sb distances < 350 pm, the averaged *MOP*s (as taken from the extended Hückel calculation) are 0.287 and 0.316 for "ZrFeSb" and "$ZrFe_{0.75}Sb$", respectively, and 0.324 and 0.345 for the Ni-containing model structures. The relative differences are approximately 10% for $M' = Fe$ and 6% for $M' = Ni$. Rather negligible differences occur in teh ratios of the averaged *MOP*s for the M'–Sb bonds with 0.278/0.279 for $M' = Fe$ and 0.205/0.205 for $M' = Ni$.

Altogether, the differences in bonding discussed above render a substoichiometry more likely in the case where $M' = Fe$ in $ZrM'Sb$, which is in agreement with the experiment. One might assume to find the same trend among the ternary Hf antimonides, the lattice parameters of which showing almost isotropical contractions, compared to ZrFeSb as well as ZrNiSb. A more sophisticated discussion, however, would result if one could also consider the bonding interactions of the competing phases, which are still unknown inthe ternary Zr/Fe/Sb system.

SUMMARY

Among the equiatomic antimonides, no differences have yet been found between the structure types of the Zr and Hf

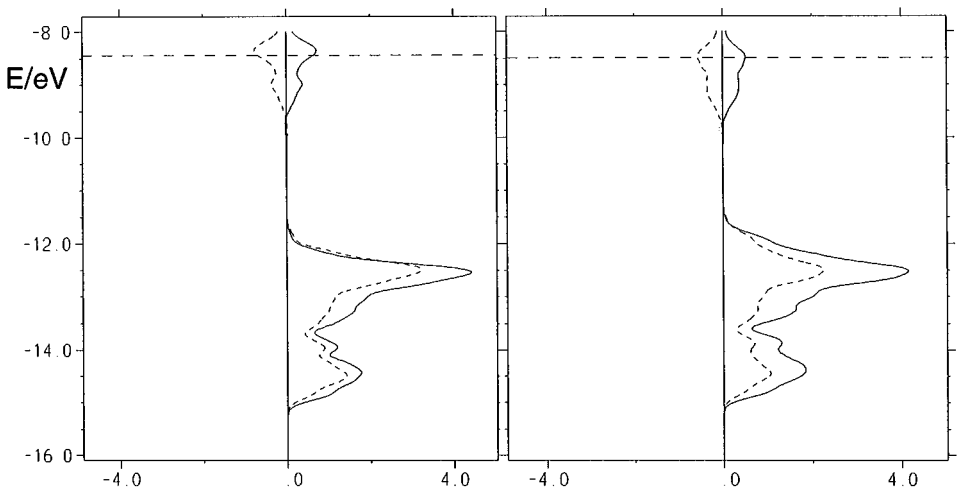

FIG. 7. Summed crystal orbital overlap populations (COOP) for "ZrFeSb" (left) and "$ZrFe_{0.75}Sb$" (right) (EH results). Horizontal lines: Fermi levels. Solid line, Zr–Sb; dashed line, Fe–Sb interactions. Left, antibonding (–); right, bonding (+).

antimonides. $ZrFe_{1-x}Sb$ crystallizes like ZrNiSb and $ScCo_{1-x}Sb$ in the TiNiSi structure type, whereas TiFeSb occurs in the LiAlSi type. In contrast to ZrNiSb, the 3*d* metal atom site of $ZrFe_{1-x}Sb$ cannot be filled completely under the reaction conditions used. A rather small phase range, if any, was confirmed via single crystal studies to be within $0.32(1) \leq x \leq 0.37(1)$. On the other hand, the phase range of $ScCo_{1-x}Sb$ includes at least $0.07(1) \leq x \leq 0.25(1)$. $ZrFe_{1-x}Sb$ should be metallic and exhibit Pauli paramagnetic behavior, according to the results of the calculations of the electronic structure, independent of the iron deficiency.

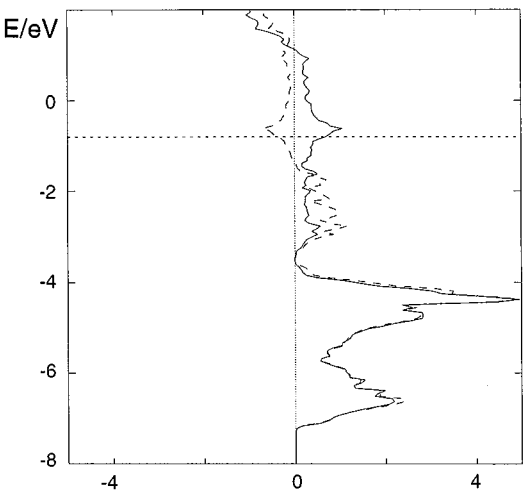

FIG. 8. Summed crystal orbital Hamilton populations (–COHP) for "ZrFeSb" (LMTO results). Horizontal line: Fermi level. Solid line, Zr–Sb; dashed line, Fe–Sb interactions. Left, antibonding (–); right, bonding (+).

ACKNOWLEDGMENTS

Financial support of the Deutsche Forschungsgemeinschaft, the Fonds der Chemischen Industrie, and the Bundesministerium für Bildung, Wissenschaft, Forschung und Technologie is gratefully acknowledged. Fruitful discussions with Bernd Harbrecht are appreciated.

REFERENCES

1. P. I. Krypyakevich and V. Y. Markiv, *Dopov. Akad. Nauk Ukr. RSR* (**12**), 1606 (1963).
2. H. Kleinke, *Z. Anorg. Allg. Chem.* **624,** 1771 (1998).
3. V. K. Pecharski, Y. V. Pankevich, and O. I. Bodak, *Sov. Phys-Cryst.* (Transl. from Kristallogr.) **28,** 97 (1983).
4. A. E. Dwight, *Proc. Rare Earth Res. Conf.* **2,** 642 (1974).
5. K. Hartjes and W. Jeitschko, *J. Alloys Compd.* **226,** 81 (1995).
6. R. Marazza, R. Ferro, and G. Rambaldi, *J. Less-Common Met.* **39,** 341 (1975).
7. C. B. H. Evers, C. G. Richter, K. Hartjes, and W. Jeitschko, *J. Alloys Compd.* **252,** 93 (1997)
8. H. Kleinke, *Z. Anorg. Allg. Chem.* **624,** 1272 (1998).
9. A. H. El-Sayed, G. J. Niewenhuys, J. A. Mydosh, and K. H. J. Buschow, *J. Phys.* **F18,** 2265 (1988).
10. S. K. Malik and D. T. Adroja, *Phys. Rev.* **43B,** 6295 (1991).
11. O. Trovarelli, J. G. Sereni, G. Schmerber, and J. P. Kappler, *Phys. Rev.* **49B,** 15179 (1994).
12. R. V. Skolozdra, J. F. Mikhalski, K. Kaczmarska, and J. Pierre, *J. Alloys Compd.* **206,** 141 (1994).
13. S. Ögüt and K. M. Rabe, *Phys. Rev.* **B51,** 10443 (1995).
14. C. Hordequin, J. Pierre, and R. Currat, *J. Magn. Magn. Mater.* **162,** 75 (1996).
15. Stoe & Cie GmbH, XRED/XSHAPE, Darmstadt, Germany, 1996/1997.
16. G. M. Sheldrick, SHELXL-97, Universität Göttingen, Germany, 1997.
17. R. Hoffmann, *J. Chem. Phys.* **39,** 1397 (1963).
18. M.-H. Whangbo and R. Hoffmann, *J. Am. Chem. Soc.* **100,** 6093 (1978).
19. Program, EHMACC, adapted for use on a PC by M. Köckerling, Gesamthochschule Duisburg, 1997.

20. U. van Barth and L. Hedin, *J. Phys.* **C4,** 2064 (1971).
21. O. K. Andersen, *Phys. Rev.* **B12,** 3060 (1975).
22. H. L. Skriver, "The LMTO Methods." Springer, Berlin, 1984.
23. O. Jepsen and O. K. Andersen, *Solid State Commun.* 9 (1971).
24. L. Pauling, "The Nature of the Chemical Bond," 3rd ed. Cornell Univeristy Press, Ithaca, NY, 1948.
25. C. J. Bradley and A. P. Cracknell, "The Mathematical Theory of Symmetry in Solids." Clarendon Press, Oxford, 1972.
26. T. Hughbanks and R. Hoffman, *J. Am. Chem. Soc.* **105,** 3528 (1983).
27. R. Dronskowski and P. E. Blöchl, *J. Phys. Chem.* **97,** 8617 (1993).
28. H. Kleinke and H. F. Franzen, *Z. Anorg. Allg. Chem.* **624,** 51 (1998).
29. H. Kleinke and H. F. Franzen, *Z. Anorg. Allg. Chem.* **622,** 1893 (1996).